PNAS Nexus, 2023, 2, 1–13
https://doi.org/10.1093/pnasnexus/pgad232
Advance access publication 24 July 2023
Research Report

Engineering confined fluids to autonomously assemble hierarchical 3D structures

Oleg E. Shklyaev, Abhrajit Laskar and Anna C. Balazs*

Department of Chemical & Petroleum Engineering, University of Pittsburgh, 3700 O'Hara Street Benedum Hall of Engineering, Pittsburgh, PA 15261, USA
*To whom correspondence should be addressed: Email: balazs@pitt.edu
Edited By: Cristina Amon

Abstract

The inherent coupling of chemical and mechanical behavior in fluid-filled microchambers enables the fluid to autonomously perform work, which in turn can direct the self-organization of objects immersed in the solution. Using theory and simulations, we show that the combination of diffusioosmotic and buoyancy mechanisms produce independently controlled, respective fluid flows: one generated by confining surfaces and the other in the bulk of the solution. With both flows present, the fluid can autonomously join 2D, disconnected pieces to a chemically active, "sticky" base and then fold the resulting layer into regular 3D shapes (e.g. pyramids, tetrahedrons, and cubes). Here, the fluid itself performs the work of construction and thus, this process does not require extensive external machinery. If several sticky bases are localized on the bottom surface, the process can be parallelized, with the fluid simultaneously forming multiple structures of the same or different geometries. Hence, this approach can facilitate the relatively low-cost, mass production of 3D micron to millimeter-sized structures. Formed in an aqueous solution, the assembled structures could be compatible with biological environments, and thus, potentially useful in medical and biochemical applications.

Significance statement

The challenge of self-assembling micron-scale objects is spurring development of alternative approaches to spontaneous structure formation. Using modeling, we devise an approach that harnesses the coupling between chemical and mechanical energy within fluid-filled chambers to autonomously assemble hierarchical, millimeter-sized 3D structures. Catalytic reactions in the solution produce local variations in chemical concentration, which produce mechanical forces (i.e. chemo-mechanical transduction). The forces generate vortices comprising flows both parallel and perpendicular to the confining walls. These orthogonal streams can be manipulated independently, allowing the patterning of fluid flows to assemble 2D, horizontal panels into robust 3D morphologies. The assembly is tolerant to degrees of randomness in the initial panel placement, enabling the fluid-driven formation of regular tetrahedrons, prisms, and cubes.

Introduction

Chemical reactions within fluid-filled microchambers naturally produce distinct thermal and chemical gradients within the solution; these gradients inherently generate forces that propel the spontaneous flow of the confined fluid. The fluid flow can be harnessed to perform useful mechanical work, such as transporting and organizing objects dispersed in the solution. The particular work performed by the flow depends on the nature of the generated gradients. For example, diffusioosmotic flow is instigated by gradients in chemical concentration formed near a wall and the associated interfacial forces drive the fluid parallel to the surface. Conversely, buoyancy mechanisms, either solutal or thermal, drive the flow in response to local density gradients that appear throughout the bulk of the chamber. If both these mechanisms are present, then the two flow profiles can be manipulated independently and provide a precise means of controlling the motion and work accomplished by the system. The control can be achieved by manipulating material properties of the bulk solution and the confining walls. Herein, we develop computational models to show that the generated flows autonomously assemble dispersed 2D panels into robust 3D structures. Notably, the assembled μm to mm scale 3D structures offer greater functionality than the constituent parts. Nevertheless, the coordination of intrinsic surface and bulk flows to self-organize multi-component mixtures has not been extensively utilized. Thus, a potentially powerful tool for microfabrication remains relatively unexplored.

Due to the bounding hard walls of the chamber, the flow forms convective vortices that have two distinct regions (Fig. 1), where the fluid velocities are predominantly directed parallel or perpendicular to the confining walls. Consequently, the assembly process described below can be broken into two stages. The first stage is largely controlled by the flow with velocities parallel to the bottom wall. Here, fluid flow gathers the 2D panels until

Competing interest: The authors declare no competing interest.
Received: June 22, 2023. **Revised:** June 22, 2023. **Accepted:** July 22, 2023

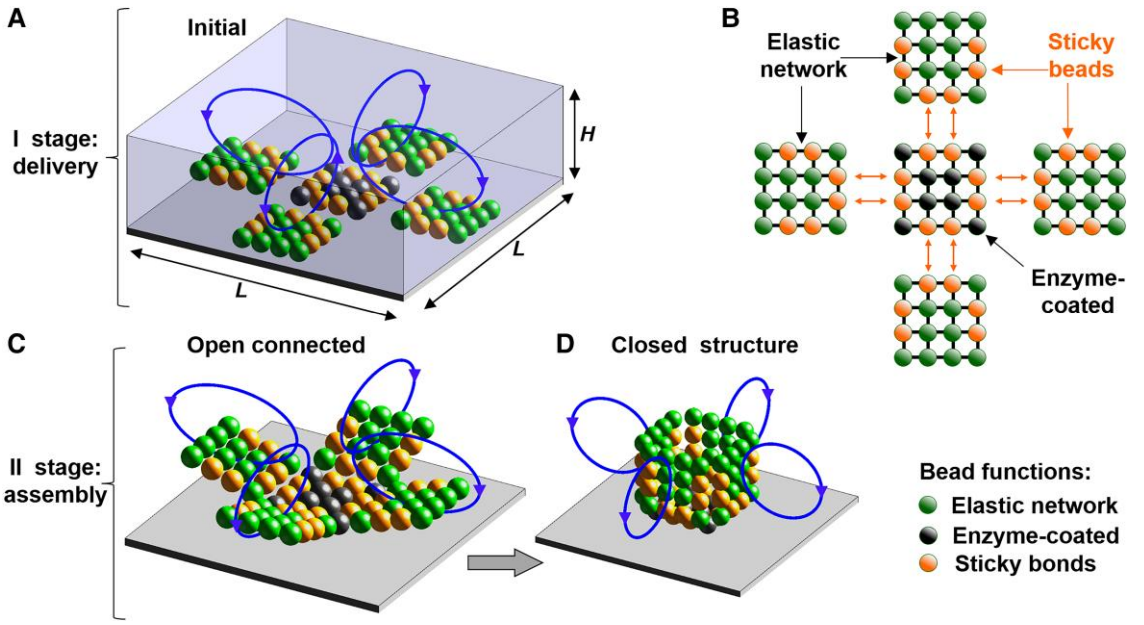

Fig. 1. Fluid flows deliver square 2D panels together and assemble them into 3D cube. A) Schematic of the fluidic chamber where disconnected square panels are dragged by the flow (blue circular lines) to the center. B) Each panel contains 16 subunits (green spheres) connected together by elastic bonds (black lines). Subunits have functionalities: green—form elastic network; orange—enable bonding between the panels; black—catalyze chemical reactions that drive fluid flows. C) After binding to the central (black) square, the side panels are dragged upward by the flow. D) Side sticky bonds lock the cubic structure.

they are within range to bind into a single 2D sheet, with well-delineated hinges. The second stage is chiefly regulated by the flow with velocities perpendicular to the wall namely, the fluid drag prompts the hinges to fold the sheet into regular 3D geometries, e.g. tetrahedrons, prisms, and closed boxes. Thus, the fluid itself spontaneously performs the work to controllably construct hierarchically shaped assemblies. Moreover, the interplay between the bulk, solutal, and interfacial, diffusioosmotic, flow mechanisms enables to design flow patterns suitable to assemble specific structures.

In contrast to the above approach, which takes advantage of innate, naturally occurring processes, researchers have devised effective methods that harness external stimuli to direct self-organization in fluidic environments. For example, with the application of the appropriate stimulus, techniques that involve origami-like cuts (1), shape-memory polymers (2, 3), stress-responsive (4, 5) multilayers (6) can drive the materials to self-fold and assemble into micron-scale 3D structures. (The latter responsive structures have been used for robotic systems (7), biomedical applications (8–10), sensors (11–14), and drug delivery systems (15).) These approaches often require the preparation of "programable" 2D layers that are cut into the final, global shapes, which might be difficult to manipulate within the fluidic environment due to relatively large viscous forces.

In the fluidic environment, the maneuvering and delivery of immersed objects can be performed by means of magnetic, acoustic, optical tweezers, or different fluidic devices. Consequently, the flows can transport microscopic objects to prescribed locations (16–19). Moreover, systems of inlets and outlets can be utilized to deliver, orient, and assemble parts into the desired structures (20, 21). Assembly via these fluidic jets requires fabrications of elaborated microfluidic chambers with systems of inlets and outlets that could be costly to produce at micron scales.

Approaches involving DNA-origami techniques provide means to bind the assembled subunits into a single structure (22). These structures could be transformed into 3D shapes (such as tetrahedrons, prisms, and cubes) with a high degree of precision and control (23, 24). Application of DNA that contains protein coiled-coil dimers provide especially efficient way of joining separate nanostructures (25). Alternatively, polymeric brushes with overlapping chains that form labile bonds (26) can be used to bind the complementary subunits and built the structure.

Below, we demonstrate how the combination of intrinsic mechanisms, such as diffusioosmosis and solutal buoyancy, can provide spontaneous fluid flows that transport materials within the chamber (27, 28) and transform 2D layers into 3D structures (29, 30). The edges of the 2D constituent sheets are decorated with complementary bonding sites (encoded either via appropriate DNA residues or labile bonds) that enable them to bind in a preprogramed order. These studies reveal how the fundamental conversion of chemical energy into mechanical work can be harnessed as a key design element, which can be "programed" to realize directed, autonomous fabrication in fluids.

Model

The fluid flows chemically generated in a closed microchamber can transport components and drive the assembly of microscopic structures as it is schematically illustrated in Fig. 1 (see also Supplementary Schematic S1). Initially separated 2D layers (made of interconnected green beads) of the appropriate shapes are dragged by the flow toward the base in the center (Fig. 1A) that catalyzes (black beads) chemical reactions and induces fluid motions. Upon binding to the base via sticky bonds, which decorate orange beads, the panels are dragged upward by the convective vortices shown as blue circular lines (Fig. 1C). In the upright position, the side panels are locked into a cubic structure by the additional set of side sticky bonds (Fig. 1D).

The fluid flows are generated by two independent mechanisms produced by the chemical reactions in the solution: the

diffusioosmosis and solutal buoyancy. Both mechanisms drive fluid flows in response to heterogeneous chemical concentrations produced either by the localized reactions or designed through an arrangement of chemical sources and sinks. The contribution of each mechanism in the behavior of the fluidic system depends on a range of the control parameters. Consequently, there are conditions when one mechanism dominates the other or both play comparable roles.

The submerged membranes are treated within a coarse-grained approximation where each elastic sheet is divided into a single-layer network of N_B subunits (green or orange spheres in Fig. 1) interconnected by elastic springs (black lines in Fig. 1B). Each subunit is described by the coordinates $\mathbf{r}_i = (x_i, y_i, z_i)$, $(i = 1 \ldots N_B)$ and orientations (as discussed in the Supplementary Note S1). Relative motion of the subunits causes distortions in the elastic network. The associated changes in the elastic energy E produce local forces $\mathbf{F}^{\text{elastic}}(\mathbf{r}) = -\frac{\partial E}{\partial \mathbf{r}}$ directed to flatten the sheet to its equilibrium configuration. The characteristic radius R of the subunits (spherical beads) represents a half-thickness of the elastic sheet. The steric interactions between the beads $\mathbf{F}^{\text{steric}}(\mathbf{r}) = -\frac{\partial U^{\text{steric}}}{\partial \mathbf{r}}$ are modeled via the Morse potential $U^{\text{steric}} = \varepsilon(1 - \exp[-\omega(r - r_0)])^2$, where parameters ε, ω, and $r_0 = R$ specify the respective strength and width of the interaction, and the equilibrium distance. The density of the subunits ρ_b is assumed to be greater than that of the host solution ρ_0. Therefore, in the absence of fluid flows each bead sediments to the bottom of the chamber due to the gravity force $\mathbf{F}^{\text{gravity}} = 4\pi R^3(\rho_b - \rho_0)\mathbf{g}/3$ that acts in the direction of the gravity vector $\mathbf{g} = g\mathbf{e}_z = g(0, 0, 1)$.

We assume that besides the permanent elastic bonds that act within each layers, beads located on the edges can connect together neighboring sheets via different type of bonds. These beads are shown in orange in Fig. 1. The bonds between orange beads operate as flexible hinges that connect neighboring elastic layers into a single structure and allow folding of the connected pieces moved by the flow. The sticky bonds have properties different from the permanent bonds that enable the integrity of the elastic network in the inner regions ("body") of the layers (green beads). To model the "sticky" forces $\mathbf{F}^{\text{sticky}}$ arising between two bonding sites separated by distance $\mathbf{r} = \mathbf{r}_2 - \mathbf{r}_1$ and located on the neighboring sheets, 1 and 2, we use the Morse potential U^{sticky}, which is active within the cutoff distance $r \le r_0 = d_{\text{cutoff}}$ only. Action of the gluing bonds is shown schematically with orange arrows in Fig. 1B and Supplementary Fig. S2A). The sum of the forces $\mathbf{F} = \mathbf{F}^{\text{elastic}} + \mathbf{F}^{\text{steric}} + \mathbf{F}^{\text{sticky}} + \mathbf{F}^{\text{gravity}}$ acting on the beads is treated within the immersed boundary method (IBM) (31).

We further assume, that the 2D panel immobilized in the center is coated with enzymes (black beads in Fig. 1) that catalyze heterogeneous chemical reactions. Here, each constituent subunit is associated with a source that produces chemicals C_j $(i = 1 \ldots N_C)$ with a rate described by the Michaelis–Menten relation $Q_j = \frac{M_j C_j}{K_j + C_j}$, which is controlled by the corresponding Michaelis constant K_j and the reaction rate M (mol/s). The latter specifies the amount of reagent converted to product by one subunit (black bead) per unit of time. The localized chemical reactions act as chemical "pumps" that drive fluid flows via solutal buoyancy mechanism (32, 33) and/or diffusioosmosis.

The solutal buoyancy is a bulk mechanism (32) that drives fluid flows in response to a heterogeneous chemical composition of the solution. In general, the chemical mixture can contain N_C different reagents with concentrations $C_j(\mathbf{r}, t)$, $1 \le j \le N_C$. Then, the local density of the solution, $\Delta\rho = \rho_0 \sum_j \beta_j C_j$ depends on the solutal expansion coefficients $\beta_j = (1/\rho_0)\partial\rho/\partial C_j$, which describe changes in the fluid volume caused by the presence of the dissolved chemical species C_j, and density of the solution ρ_0 in the absence of the reactants. The solutal buoyancy force and produces fluid motion characterized by velocities $\mathbf{u} = (u_x, u_y, u_z)$. The mechanism insures that the denser product-rich solution locally flows downward, while less dense product-deficient fluid rises to the top. Because of the fluid incompressibility, the upward or downward flows within the fluidic container form convective vortices that can be harnessed to transport cargo and sculpt the 2D elastic sheets into different configurations (30, 34).

The diffusioosmosis (35) is an interfacial effect that accounts for the motion of the solution along the fluid/solid interface. The fluid motion is described by the velocity $\mathbf{u}_j^{\text{DO}} = \gamma_j \nabla_{||} C_j$, where $\nabla_{||} C$ denotes the concentration gradient parallel to the wall. Diffusioosmotic mobility γ_j describes details of the intermolecular interactions between the solute molecules of chemical j and the adjacent fluid/solid interfaces. The full system of equations and boundary conditions are discussed in the Section Methods.

The relative importance of the diffusioosmosis and solutal buoyancy mechanisms can be illustrated by applying the lubrication approximation (36, 37), which we discuss in the Methods and Supplementary Note S2. When the height of the domain is sufficiently smaller than its horizontal size, $H << L$, the approximation yields the velocities (Eq. 10) of fluid flows driven by the appropriate chemical gradients $\partial_r C$. The relative contributions of the solutal buoyancy and diffusioosmosis mechanisms are controlled by the respective dimensionless numbers $\text{Gr} = \frac{g H^3 L |\beta|}{\nu^2} \nabla C^*$ and $\Gamma_\alpha = \frac{\gamma_\alpha H}{\nu} \nabla C^*$ that couple fluid velocity to the gradient $\partial_r C$. (In the latter expression, $\alpha = 0$ at the bottom and $\alpha = 1$ at the top wall.) Given that the channel height is H, the scaling of the dimensionless numbers $\text{Gr} \propto H^3 \nabla C^*$ and $\Gamma_\alpha \propto H \nabla C^*$ indicates the dominant mechanisms controlling the fluid flow, which imply that the corresponding dimensionless velocities scale as $u_r \propto \text{Gr} \propto H^3$ or $u_r \propto \Gamma_\alpha \propto H$ (see Eq. 10). For a sufficiently narrow chamber, the fluid propulsion is dominated by diffusioosmosis controlled by Γ_α. Hence, flow produced by a confining surface governs the dynamic behavior of the system. (Basic examples of diffusioosmotic flows produced by the bottom and top surfaces are shown in Supplementary Fig. S1.) Conversely, for a sufficiently large H, the flow is generated in the bulk of the fluid by the buoyancy mechanism (controlled by Gr) that plays the major role in the system's dynamics. Experiments (38–40) in channels with a characteristic thickness H~10 microns illustrate that diffusioosmosis can propel fluid with velocities on the order of 1~10 μm s^{-1}. In larger domains (H), experiments with catalytic pumps operating in chambers with thicknesses H~1 mm, demonstrate (41) that buoyancy-driven flows can reach velocities 1~10 μm s^{-1}. The scaling of the respective governing parameters $\propto H^3$ and H suggests the existence of a region where the two mechanisms of fluid propulsion play comparable roles. Namely, in microchannels with characteristic dimensions $10\,\mu\text{m} < H < 1\,\text{mm}$, both mechanisms can produce flows with comparable velocities and the two mechanisms could be combined to design flow patterns with desirable properties.

Results and discussion

To illustrate the principles of our approach, we first consider profiles of the fluid flow produced by the solutal buoyancy and

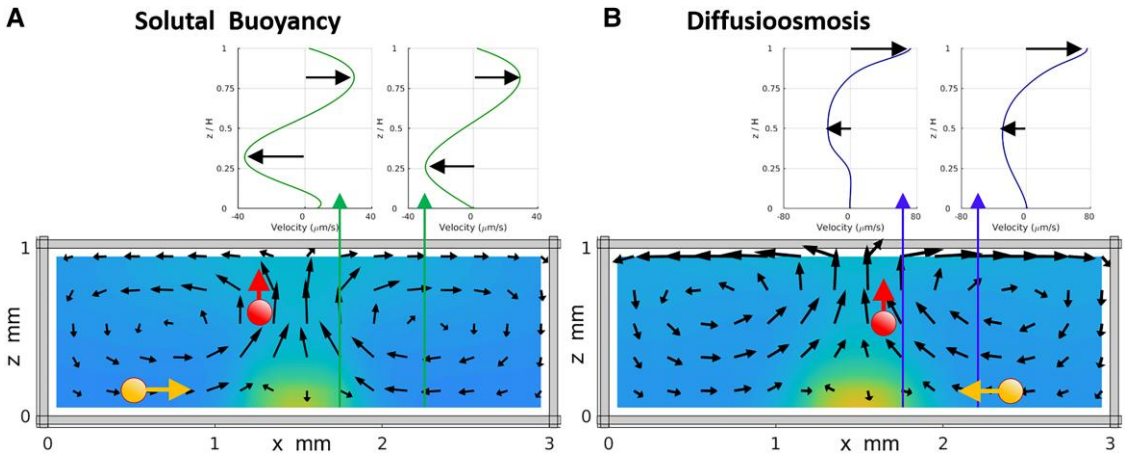

Fig. 2. Fluid flows generated via the solutal buoyancy (A) and diffusioosmosis (B). Black arrows illustrate the flow field $\mathbf{u}(x, y = L/2, z)$. The insets on the top show horizontal fluid velocities $u_x(x, y = L/2, z)$ at specific locations x. Chemicals produced in the center of the domain are shown with yellow color map. Yellow beads at the bottom are dragged by the flow in the horizontal direction toward the center. Red beads in the center+ are dragged in the vertical direction.

diffusioosmotic mechanisms in the absence of submerged objects. In both cases, chemical reactions catalyzed at the center of the bottom wall (color map in Fig. 2A and B) produce radial density variations that drive radial fluid flows. The patterns of the fluid velocities, shown with black arrows, illustrate the flow profiles in a mid-plane ($y = L/2$) of the simulation domain. Figure 2A shows the profile for flow driven *via* the solutal buoyancy mechanism. The typical horizontal velocity profiles $u_x(z/H)$ have an S-like shape and zero velocity at the bottom and top of the domain. Figure 2B shows the profile for flow driven *via* diffusioosmosis. The flow profiles $u_x(z/H)$ feature zero velocities at the bottom wall; chemical gradients generate the flow at the top wall of the chamber, i.e. $\mathbf{u}_x(z = H) = -\Gamma\nabla_{||}C$, where the velocities reach their maximal values.

Gauge beads

To understand the effect of the fluid flow on the submerged structures, we first consider forces acting on a single "gauge" bead (i.e. so named because it is used to gauge the effects of the local environment). By focusing on a single bead rather than a network of interconnected beads, we can decouple the hydrodynamic forces imposed by the flow from the elastic forces arising from deformations in the network. To gain the most insight into the hydrodynamic effects, these beads are placed in specific regions of the flow that contribute different essential forces to the assembly process. (As an aid to the eye, the gauge beads are marked in different colors to distinguish their particular locations in the chamber.) Independent of the initial position (yet sufficiently far from the center), all stationary yellow beads on the bottom wall experience radial drag forces imposed by the flow. The forces drive the beads toward the center where they serve as building blocks in the subsequent construction.

In the central region, the upward flow above the catalytic site imposes a vertical drag force $f = 6\pi R\eta\mathbf{u}$ on a fixed red bead. This region of the flow is particularly effective in driving structural elements in the vertical direction. Notably, the drag forces that act on a given bead generated through both the solutal buoyancy (Fig. 2A) and diffusioosmosic effects (Fig. 2B), display similar directionalities. As we demonstrate below, the situation changes in the presence of the mobile, submerged 2D panels of interlinked beads (which substantially change the flow patterns). Then, the contributions from buoyancy-driven and diffusioosmotic flows are quite distinct and allow us to tailor the flow patterns to achieve successful assembly processes.

Structural elements formed from interlinked beads are placed in the chamber, as shown in Fig. 1. Four panels are symmetrically arranged around the central, immobile enzyme-coated base (black beads). We use the attractive part of the Morse potential to model the presence of chemically functionalized "sticky" beads (shown in orange), which form bonds with "sticky" beads on neighboring panels (indicated with orange arrows in Fig. 1B). These functionalized beads enable different sheets to bind into a single structure that is connected *via* flexible hinges.

The success of the assembly process depends on the precision in the initial arrangement of the panels (with total number N_p). To quantify deviations from perfect placement that display the four-fold symmetry (gray curbed panels in Supplementary Fig. S2B), we introduce parameters $(d_j, \Delta\theta_j, \varphi_j), j = 1 \ldots N_p$. Here, d_j and $\Delta\theta_j = \theta_j - \theta_j^0$, are the respective radial distance from the central location to the side panels and polar angles that specify the location of the j-th side panel in the polar coordinates; φ_j is an in-plane rotation angle. The perfect cubical structure ($N_p = 4$) has four-fold symmetry with $d_j^0 = d$, $\varphi_j^0 = 0$, and $\theta_j^0 = j\pi/N_p$. Examples of the displaced panels are shown as darker gray squares and the latter notion is used below to quantify the degree of precision needed to successfully assemble the 3D structures.

In these studies, the 3D structures formed from these 2D panels encompass simple geometries, such as a tetrahedron, prism, and rectangular box. (Below, we use the words "panels" and "sheets" interchangeably.) Initially, the reactant concentration, $C(t = 0)$, is homogeneous throughout the fluid-filled microchamber. Flexible sheets of a specific shape are placed on the bottom of the chamber and the edges of each sheet are assumed to be decorated with reactive binding sites (Fig. 1), which provide the necessary adhesive interactions. The central sheet is fixed in place and coated with enzymes that catalyze the chemical reaction.

The successful fluidic assembly involves the following main ingredients. First, the immobile enzyme-coated base that catalyzes chemical reactions and produces the fluid motion should be placed sufficiently close to the points of special symmetry of the system, such as the center of the fluidic domain in case of one assembled structure. The arrangements of the side mobile panels around the immobile base should enable the complementary

neighboring panels to approach one another and make contacts via dynamical sticky bonds. Therefore, there are ranges of parameters that enable the described strategy to work. The deviations from the most favorable conditions reduce chances of the successful assembly. The effects of possible imperfections on the process of assembly and permissible ranges of the control parameters are discussed in the Supplementary Note S3.

Assembly processes involving just the solutal buoyancy mechanism

We first consider scenarios that involve only solutal buoyancy. When the products of the reaction are less dense than the reactants, the density variations produced about the central, immobile sheet generate upward fluid motion, with the fluid velocities being perpendicular to the bottom wall. In the closed container, the flow forms convective vortices as the upward flowing fluid reaches the top wall and then recirculates along the other walls in the chamber. Hence, flows involve not only upward motion that is perpendicular to the bottom wall but also fluid motion that lies parallel to these same walls, as indicated in Fig. 1 (see also Supplementary Fig. S6). As noted above, due to the presence of these spatially separated, essentially orthogonal flows, the assembly process can be divided into two stages. First, the generated flow transports the submerged sheets along the bottom wall toward the center, where they come in contact with the immobile base. The binding interactions ensure that the sheet is eventually oriented to maximize bond formation with this base and thereby compose a 2D layer lying parallel to the bottom surface. In this configuration, only the edges of the sheets are connected to the base and the sheets are free to be pulled upward by the fluid drag forces.

The latter action happens in the second phase, where the upward flow brings edges of the neighboring sheets into close proximity, prompting the formation of new bonds that lock the configuration of the structure. As demonstrated below, the local interactions between a given sheet and the base can occur at different times for different sheets. Hence, one sheet can be experiencing the second stage of construction, while another is still undergoing the first stage. Importantly, however, due to the action of the complementary forces and the binding interactions, the system ultimately forms a coherent 3D structure. In our simulations, we assume that the lengths of the side panels are smaller than the height, H, of the fluidic chamber. Therefore, the reorientation of the initially horizontal panels into vertical positions during the 3D assembly process does not cause collisions with the top wall of the domain.

Figure 3A–C display the robust fluid-driven construction of a tetrahedron. Three triangular sheets were initially arranged around a central triangular base at different distances from the center (Fig. 3A). To randomize positions and orientations, each triangle is rotated in its plane around the center of mass, as shown in the Supplementary Fig. S2B. We typically assigned initial deviations from the four-fold symmetry in angles $\theta_j - \theta_j^0$ and $\varphi_j - \varphi_j^0$ on the order of 10° and the radial distances from each other, d_j, could vary by as much as 50%. As the first mobile sheet (closest to the center) approaches the triangular base, the respective reactive sites (orange beads) bind to form a hinge between these two panels (Fig. 3B). The fluid moving upward in the central region drags the outer edge of the connected sheet into the upright position. Buffeted by the upward flow, the sheet remains in this position until the second sheet arrives at the base. Now, this second "petal" becomes bound to the base and is dragged by the flow to the upright position, where it becomes connected to the first sheet *via* the neighboring edges. Finally, the third petal arrives, binds to the base, and is brought to the upright position by the flow, thus completing the construction of the tetrahedron (Fig. 3C).

The same approach can be used to construct an "open" prism (Fig. 3D–F), which is formed from a triangular, anchored base and three, square side sheets. Initially, the square sheets are located at different distances from the center (Fig. 3D) and rotated at random angles $\theta_j - \theta_j^0$ and $\varphi_j - \varphi_j^0$ in the plane. As the sheets are sequentially transported toward the center, they become attached to the triangular base and are dragged by the flow into the upright position (Fig. 3E). Binding between the sides of the square sheets leads to the completed prism shown in Fig. 3F. Detailed sequences for the assembly of the tetrahedron and prism are provided in the Supplementary Figs. S7 and S8. The stepwise process of the fluidic assembly is also demonstrated in the Supplementary Videos S1 and S2.

In all these examples, the flow parallel to the surfaces operates as a "conveyor belt" that transports structural elements along the horizontal direction to the construction site, where the pieces are joined together. Then, the sheets are shaped into the final structure by the vertical component of the flow near the center. These local variations in the flow directions enable the spatial reorientation of the components and their conjunction into the final 3D structures.

The assembly of three-sided tetrahedrons and prisms is quite robust and tolerates errors in the initial placement of the surrounding sheets. As noted above, we assembled structures that displayed initial deviations from the four-fold symmetry by as much as 10° for $\theta_j - \theta_j^0$ and $\varphi_j - \varphi_j^0$ and the initial values of d_j differed by as much as 50%. It is progressively more difficult to assemble structures with a larger number of constituent components because the process requires a higher degree of coordination between the separate moving pieces. For example, in the case of an open cubic box, the assembly process is sensitive to the initial sheet placement, being relatively intolerant of starting arrangements that deviate from four-fold symmetry. Supplementary Fig. S9 displays examples of failed assemblies of an open box formed by four square sidewalls. Deviations in the initial positions of the side panels away from optimal four-fold symmetry destroy the precise timing required for the delivery and assembly of the box. Supplementary Fig. S9 shows a case where the uncoordinated arrival of the side panels to the central base is followed by the independent motion of each sheet into the upright position. As a result, the two sheets that arrive first come into contact and lock before the other two neighbors arrive, inhibiting the formation of the correct box structure. Due to the randomness in the initial placement and excluded volume interactions, one of the panels is always the last to arrive and be set in place. As a result, the entire structure is distorted as shown in the Supplementary Fig. S9B.

While the reactive binding sites on the edges of the sidewalls stabilize the assembly process (Supplementary Fig. S10), the structure nevertheless remains unstable against the buckling caused by the fluid flow that pushes the box from all sides. Even when the four panels are initially arranged with four-fold symmetry around the central base (Supplementary Fig. S10A), the final structure is distorted from that of a cube. At early times, the symmetric arrangement enables the assembly of the cubic structure shown in Supplementary Fig. S10B. As the sidewalls that were dragged upward by the flow come sufficiently close to each other, bonds between neighboring walls lead to the formation of corners, which are more rigid than the flexible walls and enable the object to withstand the distorting influence of the flow for a while. Over time, however, the structure becomes unstable and buckles into a

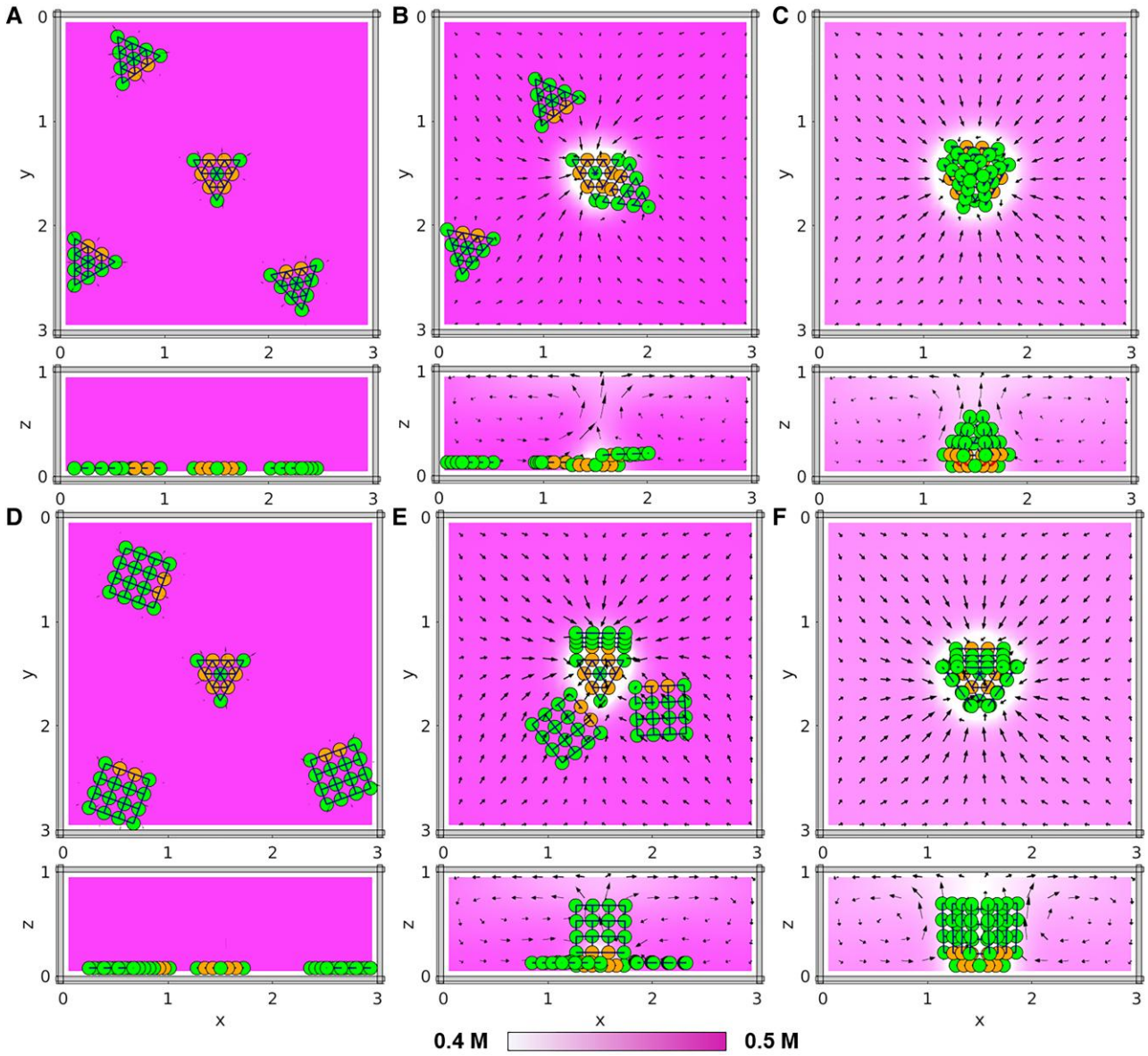

Fig. 3. Assembly of a closed tetrahedron and open prism by the convective flows. A) Initial position of the triangular base that catalyzes chemical reaction and generates flows and three triangular sheets. Binding beads are shown in orange. Color bar shows the concentration of the decomposed reactant. B) The first sheet approaches, binds to the base, and is dragged by the flow upward. C) The assembly of tetrahedron is completed. D) Initial position of the triangular base that catalyzes chemical reaction and generates flows, and three rectangular sheets around. E) The first rectangular sheet binds to the triangular base and is dragged by the flow upward. F) The assembly of prism is completed. See also Supplementary Videos S1 and S2.

construction that has either two opposite vertical corners close to each other (formed by two adjacent 2D panels) (Supplementary Fig. S10C) or two opposite sidewalls touching each other and impeding the approach of the other two walls (Supplementary Fig. S10D).

The floppy open structure, however, could be stabilized if a lid was added at the top of the box. A closed lid would fix the distance between the opposite walls and reduce the flexibility of the structure. Nevertheless, the precise closing of the top lid is a complex process that requires "engineering" the fluid flows to form the appropriate patterns.

Flow engineering: flows involving both solutal buoyancy and diffusioosmosis

To achieve more control over fluid-driven construction, we focus on designing flow patterns that provide greater temporal and spatial regulation of the submerged objects. The fluids in these systems are propelled through a combination of the buoyancy and diffusiosmotic mechanisms. Since the two mechanisms have different origins and dominate different regions of the fluid, they can be tuned independently to yield the appropriate shape of convective vortices and provide the required functionality. In particular, buoyancy-driven flows are generated in the bulk of the solution and can be designed by choosing specific chemical reactions, as well as the geometry for the microchamber. The former choice involves utilizing reagents with the appropriate expansion coefficients β [controlled by the Grashof number $\mathrm{Gr} = \frac{g r^{*3} L |\beta|}{\nu^2} \nabla C^*$ in Eq. (7)] and catalysts with the chosen turnover rate M [controlled by the Damkohler number $\Pi = \frac{M}{C^* r^* D} S$ in Eq. (8)]. In closed chambers, the structure of the buoyancy-driven flow,

however, is constrained by the boundary conditions that impose zero fluid velocities at the solid walls.

The zero velocity boundary condition at the solid walls can be lifted when the boundaries produce slip velocities, $\mathbf{u}^{DO}$ in response to chemical gradients directed along the walls, i.e. the diffusioosmic mechanism. When the container walls are coated with materials that attract or repel the solute molecules, a flow parallel to the walls is generated in response to the inhomogeneous solute concentration $\mathbf{u}^{DO} = \Gamma_\alpha \nabla_{||} C$. The combination of the flow generated in the bulk (due to solutal buoyancy) and that produced at fluid–solid interfaces (due to diffusioosmosis) can provide fluid flows with sufficiently complex patterns to enable enhanced functionality, as illustrated in Supplementary Fig. S11 and detailed in the examples below. In particular, Supplementary Fig. S11A contrasts an open box assembled exclusively *via* buoyancy-driven flows and Supplementary Fig. S11B shows a closed box folded by a combination of buoyancy-driven and diffusioosmotic flows. In the second case, the flow in the narrow gap between the top of the box and the top wall is directed toward the center (as shown with arrows) and can bring the four flaps sufficiently close to form a cover above the box. In the first case, the buoyancy-driven flow is incapable of providing such behavior.

Examples below emphasize the utility of such "engineered" flows, which are specifically designed to promote and stabilize each step of the construction. For instance, in Fig. 4, the flow is tailored not only to robustly drag the side panels horizontally toward the base of the box, and bring the attached side pieces into the upright position (Figs. 4A–D), but also to fold the triangular flaps (blue beads) at the top and thereby form a lid that secures the entire cubic structure. These triangular flaps are anchored to each mobile side panel *via* flexible elastic bonds, which operate as hinges and enable rotation of the flap with respect to the sheet. The beads at the triangular edges of each flap form the bonds needed to create a firm cover. Up to the stage in Fig. 4D, the buoyancy-driven flow performed the needed tasks. The blue flaps, however, point upward rather than folding into a lid (Fig. 4E). To accomplish the latter task, the flow must be engineered to bend the flaps toward the center in the narrow spacing above the box and below the top wall. To this end, we assume that interactions between chemicals and the material making up the ceiling generate a slip velocity $\mathbf{u}^{DO} = \Gamma \nabla_{||} C$ in response to the gradient in chemical composition produced by the localized chemical reaction. The produced diffusioosmotic flow plays the dominant role in the region near the top wall. The drag from this flow provides the force to fold the flaps and close the lid.

To illustrate the full power of the fluidic assembly, we decorate the top of each of the four panels in Fig. 5 with tentacles, as shown in Fig. 5 and Supplementary Fig. S12 with red beads. For simplicity, we assume a symmetric initial arrangements of the constituent components around the square enzyme-coated central base. In the process of folding, the structure acquires some momentum (Fig. 5D and E), which is transmitted into the clock-wise revolution of the tentacles indicated with a black arrow in panels D and E in Supplementary Figs. S12 and Fig. 5. At the final stage, shown in panel F in Supplementary Figs. S12 and Fig. 5, the assembly process is completed, all the structural elements stop moving.

Utility of diffusioosmotic flow

To highlight the distinctive role of diffusioosmosis in the construction process, we consider a mobile wheel formed from a catalyst-coated square hub (orange beads in Fig. 6) and four flexible, uncoated spokes that emanate from this central hub. The fluid here is driven exclusively through the diffusiosmotic effect produced at the top or bottom walls. We design flow patterns that show how a spinning wheel can be localized at the bottom or top wall, or in the middle of the fluidic domain (Fig. 6).

In the presence of the flowing fluid, the spokes redirect the approaching flow in the azimuthal direction and thereby generate rotation. For the case in Fig. 6A, the flow is generated *via* diffusioosmotic effects along the bottom wall. The consumption of reactants occurs at the catalyst-coated hub and forms a chemical gradient pointing away from the center. This gradient generates slip velocities $\mathbf{u}^{DO} = \gamma \nabla_{||} C$ at the bottom wall. The flow forms convective vortices (see side view) that rotate the wheel in the counterclockwise direction.

When the diffusioosmosic effect is produced at the top wall, concentration gradients formed along the wall generate slip velocity $\mathbf{u}^{DO} = \gamma \nabla_{||} C$ and flow again is directed away from the center. The resulting convective vortices lift the wheel from the bottom and pin it next to the top wall. The moving fluid (see black arrows in the side view) again rotates the wheel in the counterclockwise direction (Fig. 6C).

Finally, we assume that the properties of the top and bottom wall (characterized by γ) generate slip velocities along both the top and bottom walls directed toward the center ($\mathbf{u}^{DO} = -\gamma \nabla_{||} C$). Then, the fluid vortices near the top and bottom walls lift the wheel from the bottom and pin it in the middle of the domain. The flow coming from the top and bottom rotates the wheel in the counterclockwise direction (Fig. 6B).

The structure of the diffusioosmotic flows can also be understood by using a model based on lubrication approximation (see Supplementary information Note 2). In particular, the horizontal fluid velocities $u_x(z)$ across the fluid layer (blue lines) and streamlines that correspond to the three cases are shown in the respective panels in Fig. 6D–F. These results (fully summarized in the Supplementary Fig. S1) illustrate the influence of parameters Γ_0 and Γ_1 that govern the diffusioosmosis on the pattern of the generated flow at the respective bottom and top walls.

Parallel assembly

The fundamental concepts governing the fluidic construction of a single 3D structure can be generalized to the simultaneous assembly of multiple such objects. In particular, we show how this mechanism can be used to simultaneously assemble objects with different symmetries. In this case, special symmetry constraints need to be imposed on the design of the fluidic domain. Consider an example of the simultaneous assembly of a tetrahedron and prism (Fig. 7.) The design requires that the catalyst-coated bases of the two structures are positioned in the centers of the corresponding half domains (at $x = 1.5$, $y = 1.5$ and $x = 1.5$, $y = 4.5$). The symmetric placement of the chemically active bases permits the generation of two independent systems of fluid vortices (shown with black arrows), arranged symmetrically with respect to the central line ($x = 3$) that divides the domain into two equal parts. Due to the symmetry of the flow profiles, the horizontal fluid velocities approach zero along the middle line ($u_{||}(x = 3) \approx 0$), which effectively acts as an interface between the domains (Fig. 7). Consequently, the flow cannot drag the submerged sheets across this fluidic boundary. Mobile triangular and square sheets on the bottom wall that were initially scattered in their respective half domains are dragged by the flow toward and bind to the corresponding bases. The bound panels are dragged by the flow into the upward positions. As a result, two structures, tetrahedron and prism, are constructed simultaneously and independently at specified sites.

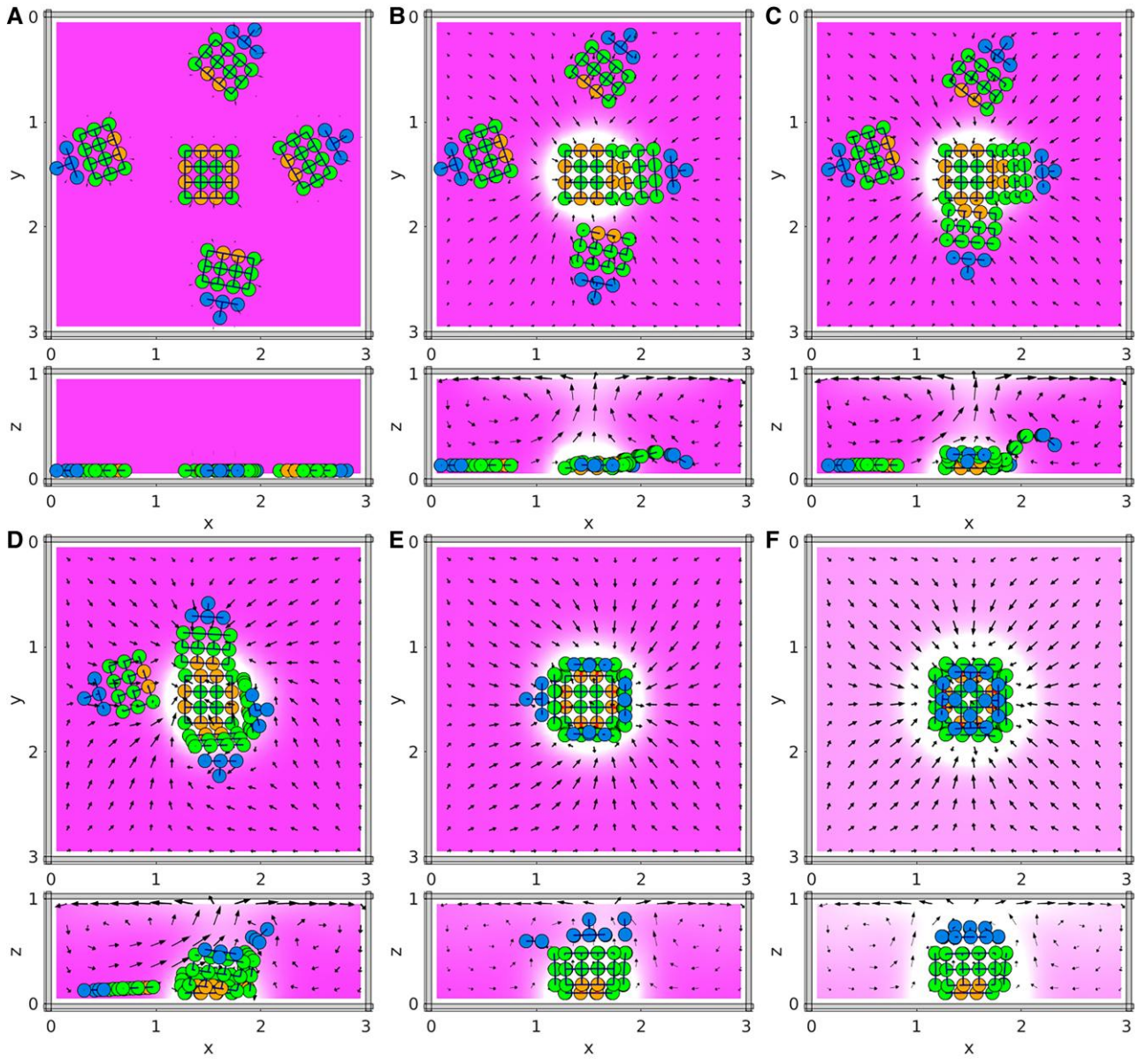

Fig. 4. Assembly of a closed box by the convective flows. A) Initial position of the rectangular base that catalyzes chemical reaction and generates flows, and four rectangular side panels. Binding beads are shown in orange. B) The first sheet approaches, binds to the base, and is dragged by the flow upward. C) The second sheet approaches, binds to the base, and is dragged upward. D) The third sheet binds to the base, and is dragged upward. E) The four side panels are assembled into an open box. F) The four blue flaps are joined to form a closed lid at the top of the box. See also Supplementary Fig. S11B (where red arrow points at the diffusioosmotic contribution of the flow that closes the lid) and Supplementary Video S3.

Supplementary Fig. S14 reveals an example where four structures, two tetrahedrons and two prisms, are assembled simultaneously. The example illustrates modes of parallel processing that are enabled by harnessing different symmetries in the system. Scale up is made possible by arranging multiple assembly sites into a regular lattice, where each fluidic "cell" operates independently. Namely, separated by boundaries where the horizontal fluid velocities are zero, $u_{||} = 0$, the fluid cannot transport elements across these barriers and each fluidic cell can be used to construct distinct microscopic objects. The latter approach provides a new route to mass production at the microscale.

Since the method relies on the symmetries of the generated flows, sufficiently large distortions in the system design can lead to defects in the final structures or disrupt the assembly process. Nevertheless, in the examples shown here, perturbations caused by the random positioning of mobile sheets were sufficiently small that the process of independent assembly was successful. Another potential source of error can arise from distortions generated by the imperfect placement of the enzyme-coated bases that generate flows. Similarly, the amount of enzyme immobilized on different bases needs to be equal for all bases of the same shape. If not, the active bases can generate unequal fluidic vortices so that the boundaries separating the independent fluidic cells are no longer straight, inhibiting this mode of parallel assembly. Effects of different types of imperfections on the assembly process are discussed in the Supplementary Note S3 and illustrated in the Supplementary Figs. S3–S5. In particular, curved boundaries separating the independent fluidic cells can be seen in Supplementary Figs. S5.

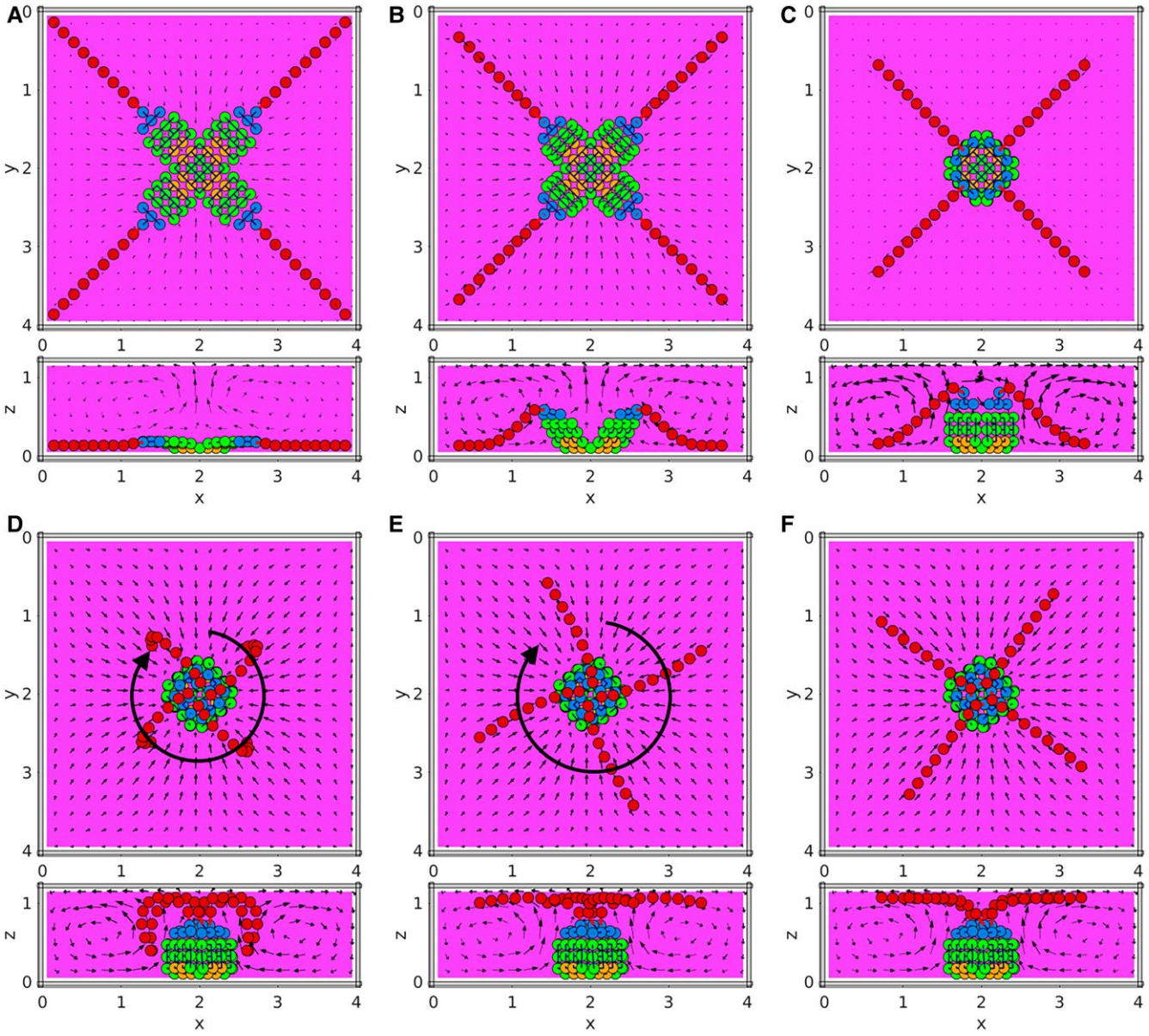

Fig. 5. Assembly of a box decorated with whiskers (red beads) on the top. The fluid flow is shown with black arrows. A) Initial position of a central rectangular base that catalyzes chemical reaction and generates flows, and four peripheral rectangular sheets with the whiskers. Binding beads are shown in orange. B) The four rectangular sheets bind to the rectangular base and are dragged by the flow upward. C) The four peripheral sheets are assembled into an open box. D) The top cover of the box (in blue) is closed up. E) The assembly of box is completed, while the whiskers revolve clock-wise. F) The assembly process is completed and all the structural elements stop moving. See also Supplementary Video S4.

Discussion

We demonstrated that the combined action of two independent, naturally occurring mechanisms in confined fluids generates the necessary fluid flows to spontaneously assemble submerged 2D layers into robust 3D structures. The generated flows are produced by forces that lie orthogonal to each other, with motion produced by diffussioosmosis being predominantly parallel to horizontal walls and motion due to solutal buoyancy generated by the vertically oriented forces. The two mechanisms can occur simultaneously in a chamber and be tailored separately. The independent control the interfacial and bulk driving forces imparts the fluid with remarkable abilities to manipulate the assembly. In particular, in the presence of the appropriate reactants to trigger the chemical reactions, the assembly process occurred autonomously, without the need for external instruction. Once the individual pieces came into sufficiently close contact, reactive binding sites on the edges of these pieces formed bonds that stabilized the structure. Hence the structures were robust and maintained their shape even in the continuing flow. Moreover, the fluid-driven assembly was tolerant to degrees of randomness in the initial placement of the parts. We demonstrated this process through the construction of tetrahedrons, prisms, and cubes in the fluidic environment. Note also, that main ingredients necessary for the experimental realization of the fluidic assembly are available at the present (see Supplementary Note S4).

Tetrahedron and prism structures were composed of a small number of parts and thus were easier to assemble and more tolerant to errors in initial placements than structures requiring a greater number of constituents (cubic boxes). Nevertheless, the addition of extra bonding sites on the aggregating parts and the

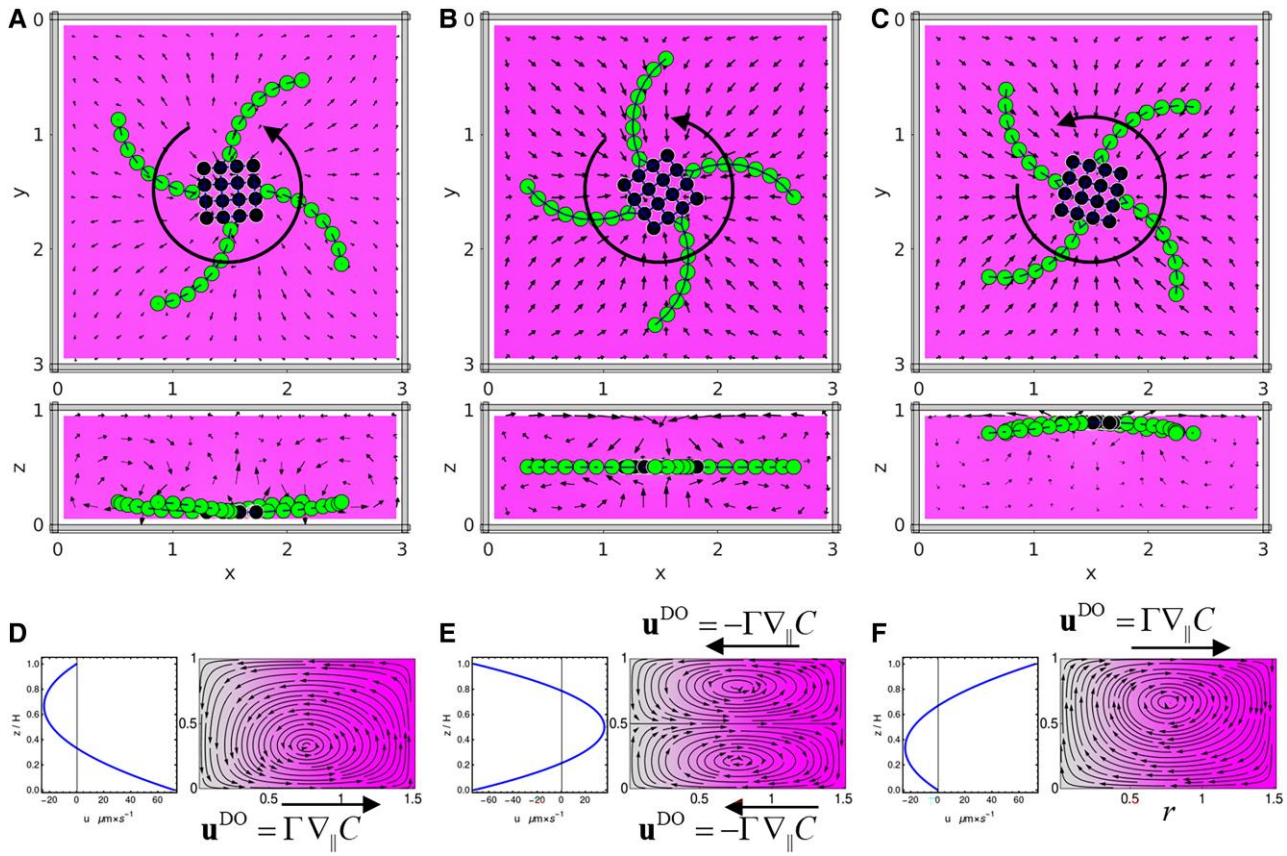

Fig. 6. Rotating wheels positioned by the flow at the bottom, middle, and top of the chamber. The chemical reaction catalyzed at the square base of the wheel (black beads) produces fluid flow (black arrow) at the top or bottom solid walls via diffusioosmotic effect. The wheel, which is immobilized in the x–y plane but is free to move along z, rotates in the counterclockwise direction (circular arrow). A) The rotating wheel is pinned to the bottom wall by the flow produced at the bottom boundary. B) Flows generated by the top and bottom wall fix the rotating wheel in the middle of the domain. C) The wheel is pinned to the top wall by the flow generated at the top boundary. The respective stream lines produced within the lubrication approximation (Supplementary Note S2) are shown in the panels (D), (E), and (F). These panels also show horizontal fluid velocities (blue lines) $u_x(z/H)$ as function of the vertical coordinate. Sequential snapshots that illustrate the dynamics of case (B) are shown in Supplementary Fig. S13. See also Supplementary Video S5.

specific flow design stabilized the process and helped to overcome the errors from the initial conditions (Fig. 4). In particular, the process of the fluidic assembly can be adjusted by designing convective flow patterns suitable for specific purposes. For instance, the closing of the lid at the top of the rectangular box was enabled through the appropriate combination of the diffusioosmosis and solutal buoyancy generated flows.

For the assembly process, the system that can be divided into a lattice of the individual fluidic cells, with each one operating independently of the neighbors. This attribute enables parallel construction of multiple units and scale up, making the system suitable for the mass production of microscale structures. We also showed that the simultaneous assembly of sheets with different geometries requires more careful design considerations since sheets of different geometries have different drag coefficients and, therefore, demonstrate different aggregation dynamics. In these scenarios, it becomes more difficult to achieve appropriate timing and coordination between the assembling blocks. Nonetheless, we demonstrated successful simultaneous assembly of the prismatic structures and tetrahedrons.

Methods

The behavior of the system, which encompasses the motion of fluid, heterogeneous chemical reactions, and assembly of the submerged objects, is simulated in a rectangular domain $\{(x, y, z): 0 \le x, y \le L,\ 0 \le z \le H\}$ bounded by solid walls. The dynamics of the system are governed by the continuity, Navier–Stokes, reaction–diffusion equations, and equations describing the mobile subunits

$$\nabla \cdot \mathbf{u} = 0, \tag{1}$$

$$\partial_t \mathbf{u} + (\mathbf{u} \cdot \nabla)\,\mathbf{u} = -\frac{1}{\rho_0}\nabla p + \nu \nabla^2 \mathbf{u} + e_z\, g \frac{\Delta\rho}{\rho_0} + \frac{1}{\rho_0}\mathbf{F}, \tag{2}$$

$$\partial_t C_j + (\mathbf{u} \cdot \nabla)\, C_j = D_j\, \nabla^2 C_j + \sum_{i=1}^{N_A} \frac{M_j\, C_j}{K_j + C_j}\, \delta(\mathbf{r} - \mathbf{r}_i), \quad 1 \le j \le N_C, \tag{3}$$

$$\partial_t \mathbf{r}_i = \mathbf{u}, \qquad i = 1..N_B. \tag{4}$$

Here, ∂_y is the derivative with respect to a variable y, ∇ is the spatial gradient operator, ν is the kinematic viscosity, and D_j is the diffusivity of reactant C_j. The density variations in solution $\Delta\rho = \rho_0 \sum_j \beta_j C_j$ depend on the expansion coefficients $\beta_j = (1/\rho_0)\partial\rho/\partial C_j$. N_B is the total number of beads. N_A is the number of active beads that constitute an immobilized, catalyst-coated central panel of each self-assembling structure. The latter beads are shown as black spheres in Fig. 1.

We introduce characteristic scales (marked with stars) and define dimensionless (primed) variables as:

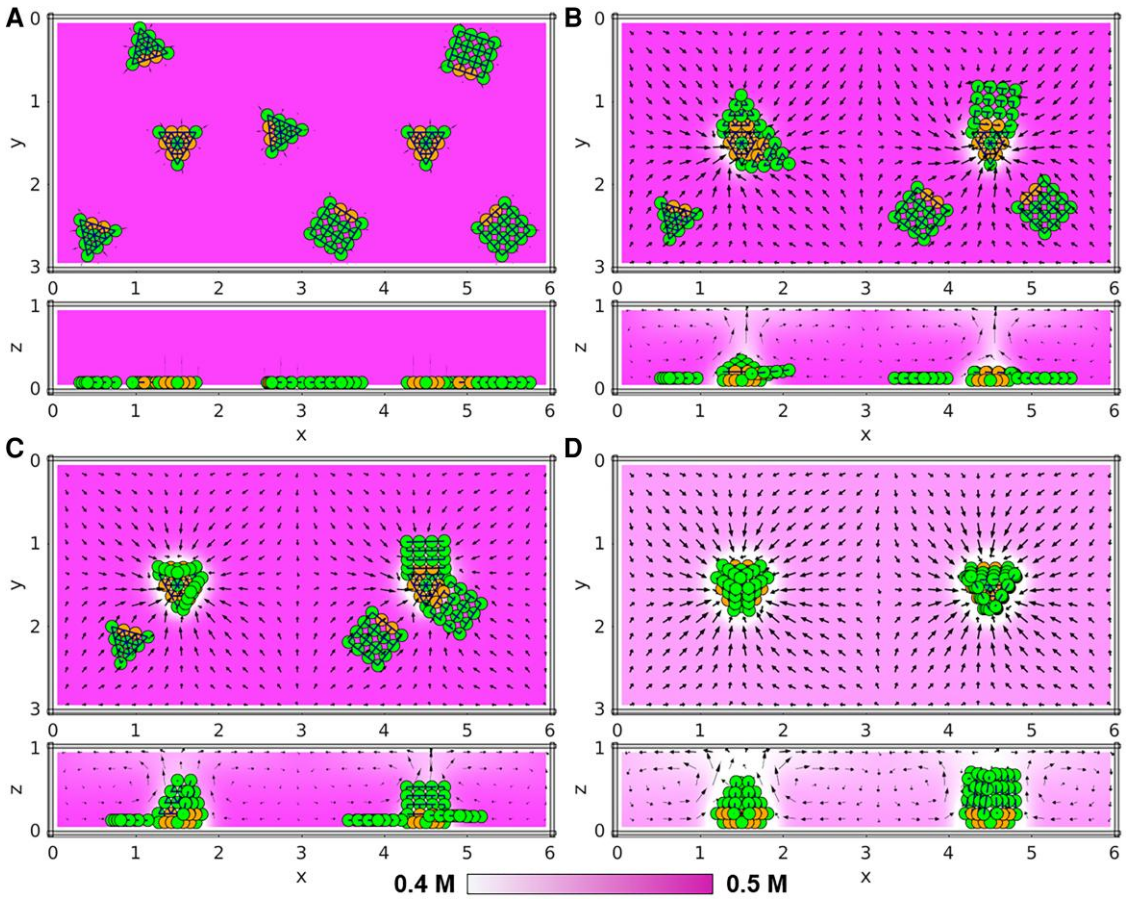

Fig. 7. Independent assemblies of tetrahedron and prism in one fluidic domain. A) Initial position of the triangular and square sheets. Immobilized triangular bases (pieces) catalyze chemical reactions (shown in white) that produce fluid flows (black arrows). The bases are located in the centers of two rectangular regions, which together constitute the entire simulation domain. Coordinates (x, y) of the left and right base are (1.5,1.5) and (4.5,15), respectively. The symmetric position of the bases with respect to the middle section at x = 3 enables symmetric flows that independently assemble two different structures: tetrahedron and prism. B) Two triangular and one square sheet are attached to the left and right base, respectively. C) The attached triangular and square sheets are dragged by the flow upward. D) The assembly of tetrahedron and prism is completed. Magenta color indicates the concentration of the reactants. See also Supplementary Video S6.

$$\mathbf{r}' = \frac{\mathbf{r}}{r^*}, \quad t' = \frac{t}{t^*}, \quad \mathbf{u}' = \frac{\mathbf{u}}{u^*}, \quad p' = \frac{t^{*2}}{r^{*2}\rho_0}p, \quad C_j' = \frac{C_j}{C^*}, \quad K_j' = \frac{K_j}{C^*}, \quad \mathbf{F}' = \frac{\mathbf{F}\,t^*}{\rho_0\,u^*}. \tag{5}$$

Dropping the primes, we rewrite the governing equations as

$$\nabla \cdot \mathbf{u} = 0, \tag{6}$$

$$\partial_t \mathbf{u} + (\mathbf{u}\cdot\nabla)\,\mathbf{u} = -\nabla p + \mathrm{N}\nabla^2\mathbf{u} + e_z \sum \mathrm{Gr}_j\, C_j + \mathbf{F}, \tag{7}$$

$$\partial_t C_j + (\mathbf{u}\cdot\nabla)C_j = \mathrm{S}_j\nabla^2 C_j + \Pi_j \sum_{i=1}^{N_A} \frac{C_j}{K_j + C_j}\delta(\mathbf{r} - \mathbf{r}_i), \quad 1 \le j \le N_C, \tag{8}$$

$$\partial_t \mathbf{r}_i = \mathbf{u}, \qquad i = 1..N_B. \tag{9}$$

We introduced the dimensionless numbers $\mathrm{N} = \frac{\nu t^*}{r^{*2}}$, $\mathrm{Gr}_j = \frac{g\,t^{*2}C^*|\beta_j|}{r^*}$, $\mathrm{S}_j = \frac{D_j\,t^*}{r^{*2}}$, $\Pi = \frac{M\,t^*}{r^{*3}C^*}$. For the viscous time scale $t^* = r^{*2}/\nu$, the numbers become $\mathrm{N} = 1$, $\mathrm{Gr}_j = \frac{g\,r^{*3}C^*|\beta_j|}{\nu^2}$, $\mathrm{S}_j = \frac{D_j}{\nu}$, $\Pi_j = \frac{M_j}{C^* r^* \nu}$. For a single chemical reaction (assumed throughout the paper), the dynamic behavior of the system is controlled by the reverse Schmidt number $\mathrm{S} = \frac{D}{\nu}$; the rate of chemical production or Damkohler number $\Pi = \frac{M}{C^* r^* D}\mathrm{S}$ (which is a ratio of the diffusive r^{*2}/D and reaction $C^* r^{*3}/M$ time scales); and the Grashof number $\mathrm{Gr} = \frac{g\,r^{*3}C^*|\beta|}{\nu^2}$, which is the ratio between the buoyancy and viscous forces. The dimensionless slip velocities $\mathbf{u}^{\mathrm{DO}} = \Gamma_\alpha \nabla_{||}\mathrm{C}$ at the bottom ($\alpha = 0$) and top ($\alpha = 1$) walls are controlled by the parameters $\Gamma_\alpha = \frac{\gamma_\alpha C^*}{\nu}$.

In the scenarios considered here, we assume that the vertical dimension, H, of the simulation domain is smaller than the horizontal dimension, L, and the chemical reactions are catalyzed in the center of the domain. The assumptions suggest that the characteristic chemical gradient ∇C^* that drives fluid motion lies along the horizontal direction. Therefore, the Grashof number and diffusioosmotic parameter can be modified to $\mathrm{Gr} = \frac{g\,r^{*3}L|\beta|}{\nu^2}\nabla C^*$ and $\Gamma_\alpha = \frac{\gamma_\alpha L}{\nu}\nabla C^*$, respectively.

To generate fluid velocities in the experimentally observed range (33, 38, 41) of ~10 $\mu m s^{-1}$, we fix the values of the following parameters to: $r^* = 10^{-3}$m, $\nu = 10^{-6}m^2s^{-1}$, $D = 1.43 \cdot 10^{-9}m^2s^{-1}$, $C^* = 1$M, $|\beta| = 0.1M^{-1}$, and the enzyme turnover rate $M/(r^*)^3 = 10^{-4}$ Ms^{-1}. The characteristic gradient becomes $\nabla C^* \sim 35\,M m^{-1}$ and the corresponding dimensionless parameters were set to $\mathrm{S} = 1.4 \cdot 10^{-3}$, $\mathrm{Gr} = 68$, $\Gamma_\alpha = 1$, and $\Pi = 10^{-4}$. The respective

bead radius and the cutoff distance of the dynamic sticky bonds were set to $R = 0.13\,r^*$ and $d_{\text{cutoff}} = 0.25\,r^*$. The respective horizontal and vertical sizes of the computational domain were set to $L = 4\,r^*$ and $H = r^*$.

Equations (6)–(9) are solved in a rectangular domain with dimensions $0 \le x, y \le L$ and $0 \le z \le H$. On the confining solid walls, the chemical fluxes are restricted from crossing these boundaries by setting $\partial_i C_j = 0$ for $i = x, y, z$ and dissolved chemical species C_j. On the vertical side walls, we impose the no-slip condition for the fluid velocities by setting $\mathbf{u} = \mathbf{0}$. At the top and bottom walls, we impose the no-slip condition for the velocity in the absence of the diffusioosmotic effect or specify the slip velocity $\mathbf{u}^{\text{DO}} = \Gamma\nabla_{||}C$ along the wall that generates fluid motion. The continuity and Navier–Stokes equations are solved using a lattice Boltzmann method (42). A finite difference approach is used to solve the diffusion equations. The IBM (31) is used to treat the fluid–structure interactions between the fluid and beads that constitute the submerged structures.

The relative importance of the diffusioosmosis and solutal buoyancy mechanisms can be readily seen in the limit of slow fluid velocities (small Gr) when the Navier–Stokes, Eq. (2), reduces to the Stokes equation $\rho\nu\,\nabla^2 u = \nabla p + \mathbf{e}_z g\,\Delta\rho$. In cylindrical coordinates (r, z), the lubrication approximation (36, 37) (Supplementary Note S2) applied to narrow chambers ($H \ll L$) provides expressions for the axisymmetric fluid flow (u_r, u_z) with velocities

$$u_r(r,z) = \left\{\frac{\mathrm{Gr}}{12}\,z(z-1)(1-2z) + \Gamma_0(1-3z)(1-z) + \Gamma_1 z(3z-2)\right\}\partial_r C, \tag{10a}$$

$$u_z(r,z) = \left\{\frac{\mathrm{Gr}}{24}\,(1-z)^2 z^2 - \Gamma_0(1-z)^2 z + \Gamma_1(1-z)z^2\right\}\partial_r^2 C. \tag{10b}$$

The expressions show that effects due to both diffusioosmosis and solutal buoyancy can arise in response to the same (or different in the case of many reagents) chemical gradient $\partial_r C$.

Acknowledgments

A.C.B. gratefully acknowledges funding from DOE under grant number DE-FG02-90ER45438. We also acknowledge the computational facilities at the Center for Research Computing at the University of Pittsburgh.

Supplementary material

Supplementary material is available at *PNAS Nexus* online.

Funding

This work was supported by DOE under grant number DE-FG02-90ER45438.

Data availability

All data are included in the manuscript and/or supporting information.

References

1 Silverberg JL, *et al.* 2014. Using origami design principles to fold reprogrammable mechanical metamaterials. *Science*. 345(6197): 647–650.
2 Lee Y, Moon J, Choi J, Cho M. 2017. Self-folding structural design using multiscale analysis on the light-absorption folding behaviour of polystyrene sheet. *Sci Rep*. 7(1):14277.
3 Mao Y, *et al.* 2015. Sequential self-folding structures by 3D printed digital shape memory polymers. *Sci Rep*. 5:13616.
4 Miskin MZ, *et al.* 2018. Graphene-based bimorphs for micron-sized, tautonomous origami machines. *Proc Natl Acad Sci USA*. 115(3):466–470.
5 Tang Y, Li Y, Hong Y, Yang S, Yin J. 2019. Programmable active Kirigami metasheets with more freedom of actuation. *Proc Natl Acad Sci USA*. 116(52):26407–26413.
6 Teshima TF, *et al.* 2017. Cell assembly in self-foldable multilayered soft micro-rolls. *Sci Rep*. 7(1):17376.
7 Kotikian A, *et al.* 2019. Untethered soft robotic matter with passive control of shape morphing and propulsion. *Sci Robot*. 4(33): eaax7044.
8 Randall CL, Gultepe E, Gracias DH. 2012. Self-folding devices and materials for biomedical applications. *Trends Biotechnol*. 30(3): 138–146.
9 Small IV W, Singhal P, Wilson TS, Maitland DJ. 2010. Biomedical applications of thermally activated shape memory polymers. *J Mater Chem*. 20(17):3356–3366.
10 Wang X, *et al.* 2022. Stimuli-responsive antibacterial materials: molecular structures, design principles, and biomedical applications. *Adv Sci*. 9(13):e2104843.
11 Breger JC, *et al.* 2015. Self-folding thermo-magnetically responsive soft microgrippers. *ACS Appl Mater Interfaces*. 7(5):3398–3405.
12 Cho JH, Hu S, Gracias DH. 2008. Self-assembly of orthogonal three-axis sensors. *Appl Phys Lett*. 93(4):1–4.
13 Guo X, *et al.* 2009. Two- and three-dimensional folding of thin film single-crystalline silicon for photovoltaic power applications. *Proc Natl Acad Sci USA*. 106(48):20149–20154.
14 Miyashita S, Meeker L, Tolley MT, Wood RJ, Rus D. 2014. Self-folding miniature elastic electric devices. *Smart Mater Struct*. 23(9):094005.
15 Fernandes R, Gracias DH. 2012. Self-folding polymeric containers for encapsulation and delivery of drugs. *Adv Drug Deliv Rev*. 64(14):1579–1589.
16 Crane NB, Onen O, Carballo J, Ni Q, Guldiken R. 2013. Fluidic assembly at the microscale: progress and prospects. *Microfluid Nanofluidics*. 14(3–4):383–419.
17 Khoo HS, Lin C, Huang SH, Tseng FG. 2011. Self-assembly in micro-and nanofluidic devices: a review of recent efforts. *Micromachines (Basel)*. 2(1):17–48.
18 Park W, Lee HS, Park H, Kwon S. 2009. Sorting microparticles by orientation using wedged-fin and railed microfluidics. TRANSDUCERS 2009—15th International Conference on Solid-State Sensors, Actuators and Microsystems 429–32.
19 Chung SE, Park W, Shin S, Lee SA, Kwon S. 2008. Guided and fluidic self-assembly of microstructures using railed microfluidic-channels. *Nat Mater*. 7(7):581–587.
20 Krishnan M, Tolley MT, Lipson H, Erickson D. 2008. Increased robustness for fluidic self-assembly. *Phys Fluids*. 20(7): 073304-1–073304-16.
21 Schneider TM, Mandre S, Brenner MP. 2011. Algorithm for a microfluidic assembly line. *Phys Rev Lett*. 106(9):094503.
22 Seeman NC, Sleiman HF. 2017. DNA nanotechnology. *Nat Rev Mater*. 3:17068-1–1706-23.
23 Rothemund PWK. 2006. Folding DNA to create nanoscale shapes and patterns. *Nature*. 440(7082):297–302.
24 Torring T, Voigt NV, Nangreave J, Yan H, Gothelf KV. 2011. Advances in DNA-based nanotechnology themed issue. *Chem Soc Rev*. 40(12):5621–5928.

25 Ljubetič A, *et al*. 2017. Design of coiled-coil protein-origami cages that self-assemble in vitro and in vivo. *Nat Biotechnol*. 35(11): 1094–1101.

26 Iyer BVS, Yashin VV, Kowalewski T, Matyjaszewski K, Balazs AC. 2013. Strain recovery and self-healing in dual cross-linked nanoparticle networks. *Polym Chem*. 4(18):4927–4939.

27 Das S, *et al*. 2017. Harnessing catalytic pumps for directional delivery of microparticles in microchambers. *Nat Commun*. 8:14384.

28 Maiti S, Shklyaev OE, Balazs AC, Sen A. 2019. Self-organization of fluids in a multienzymatic pump system. *Langmuir*. 35(10): 3724–3732.

29 Laskar A, Shklyaev OE, Balazs AC. 2021. Self-morphing, chemically driven gears and machines. *Matter*. 4(2):600–617.

30 Manna RK, Shklyaev OE, Stone HA, Balazs AC. 2020. Chemically controlled shape-morphing of elastic sheets. *Mat Horizons*. 7(9): 2314–2327.

31 Lim S, Ferent A, Sheldon Wang X, Peskin CS. 2008. Dynamics of a closed rod with twist and bend in fluid. *SIAM J Sci Comput*. 31(1): 273–302.

32 Pojman JA, Epstein IR. 1990. Convective effects on chemical waves. 1. Mechanisms and stability criteria. *J Phys Chem*. 94(12): 4966–4972.

33 Sengupta S, *et al*. 2014. Self-powered enzyme micropumps. *Nat Chem*. 6(5):415–422.

34 Laskar A, Shklyaev OE, Balazs AC. 2019. Collaboration and competition between active sheets for self-propelled particles. *Proc Natl Acad Sci USA*. 116(19):9257–9262.

35 Anderson J. 1989. Colloid transport by interfacial forces. *Annu Rev Fluid Mech*. 21(1):61–99.

36 Gentile K, *et al*. 2020. Silver-based self-powered PH-sensitive pump and sensor. *Langmuir*. 36(27):7948–7955.

37 Williams I, Lee S, Apriceno A, Sear RP, Battaglia G. 2020. Diffusioosmotic and convective flows induced by a nonelectrolyte concentration gradient. *Proc Natl Acad Sci USA*. 117(41): 25263–25271.

38 McDermott JJ, *et al*. 2012. Self-Generated diffusioosmotic flows from calcium carbonate micropumps. *Langmuir*. 28(44): 15491–15497.

39 Muraveva V, *et al*. 2022. Interplay of diffusio- and thermo-osmotic flows generated by single light stimulus. *Appl Phys Lett*. 120:231905.

40 Shin S, *et al*. 2016. Size-dependent control of colloid transport via solute gradients in dead-End channels. *Proc Natl Acad Sci USA*. 113(2):257–261.

41 Valdez L, Shum H, Ortiz-Rivera I, Balazs AC, Sen A. 2017. Solutal and thermal buoyancy effects in self-powered phosphatase micropumps. *Soft Matter*. 13(15):2800–2807.

42 Guo Z, Zheng C, Shi B. 2002. Discrete lattice effects on the forcing term in the lattice boltzmann method. *Phys Rev E*. 65(4):046308.